

Chapter 1

Introduction

This chapter provides an overview of the context in which the topics covered by this dissertation are inserted. First, a brief description of the classes of materials under investigation (dielectrics and correlated materials) and of the timescale to be addressed to achieve an ultrafast light-assisted manipulation of their optical properties is reported. Then, some experimental achievements demonstrating how a suitable light excitation can be exploited to induce new functionalities in solid-state systems are discussed. The selected examples belong to two manipulation categories: light-geometry coupling (in which the geometry of the system, together with the external light excitation, contributes to the enhancement of the optical properties) and coherent control (in which the phase of the external electric field represents an additional parameter to control the material response).

1.1 Towards Ultrafast Manipulation of New Functionalities in Solid-State Materials

The key role played by light sciences and optical technologies in providing effective solutions to worldwide challenges (such as sustainable development, energy and community health) led the United Nations to proclaim 2015 as the International Year of Light and Light-based Technologies (IYL2015¹) [General Assembly, 2013]. In this perspective, the route towards a sustainable and safe society in the future has to deal with three main challenges:

¹<https://www.light2015.org/Home/About.html>

development of low-level dissipating electronics to reduce the request of energy, implementation of more efficient energy-harvesting functionalities (from light, chemical energy or thermal energy to electricity), and the realization of secure computing and communication systems endowed by high-level performances [Tokura et al., 2017]. In this direction, among the most promising platforms, correlated materials [Tokura et al., 2017] and high-index semiconductors/dielectrics [Shcherbakov et al., 2015, Shcherbakov et al., 2017] represent good candidates for the development of devices with new functionalities.

On one hand, correlated materials represents a wide class of compounds in which the interaction between charge, orbital, and spin degrees of freedom give rise to a variety of intriguing phenomena, like insulator-to-metal transitions (IMTs), high-temperature superconductivity, topological superconductivity, colossal magnetoresistance, giant magnetoelectric effect, and topological insulators [Tokura et al., 2017]. In these compounds, characterized by partially filled $3d$, $4d$, and $4f$ orbitals, the competition between carrier localization (electron correlation) and delocalization (hopping) mechanisms is such that the low-temperature insulating phase, named *Mott insulator* (see Sec. 1.4 for a better description), arises since the Coulomb repulsion between electrons overcomes their kinetic energy, thus hindering the hopping through the lattice [Zhou and Ramanathan, 2015]. Consequently, in these compounds, the transition between the metallic and correlation-driven insulating phase (named *Mott Transition*, [Imada et al., 1998, Tokura, 2003]) is characterized by a gigantic variation of electrical conductivity, magnetic, and optical properties [Tokura et al., 2017]. The main advantage of the Mott transition, which can be manipulated by several control parameters (chemical doping, external electric field, pressure, and photo-excitation), resides in its potential implementation as electrical control in integrated circuits for non-volatile ReRAM (Resistance Random Access Memory) endowed by higher density integration, speed (at least three orders of magnitude faster than current semiconductor-based devices [Giannetti et al., 2016]), and energy savings [Tokura et al., 2017].

On the other hand, the challenge towards the development of all-optical signal processing protocols in photonics favoured the spread of high-index semiconductor and dielectric materials as main constituents in the realization of optical metasurfaces (two-dimensional structures with sub-wavelength building blocks) allowing for light fields manipulation originating from a suitable control of the optical response of the device *via* phase change [Paik et al., 2014], mechanical tuning [Ou et al., 2011], and light excitation [Fang et al., 2014, Shcherbakov et al., 2015, Shcherbakov et al., 2017]. In particular, these compounds represent a versatile alternative to metals (previously widely employed) for two main reasons: *i*) the possibility to achieve refractive index modulation due to free-carrier injection, which becomes very efficient in the

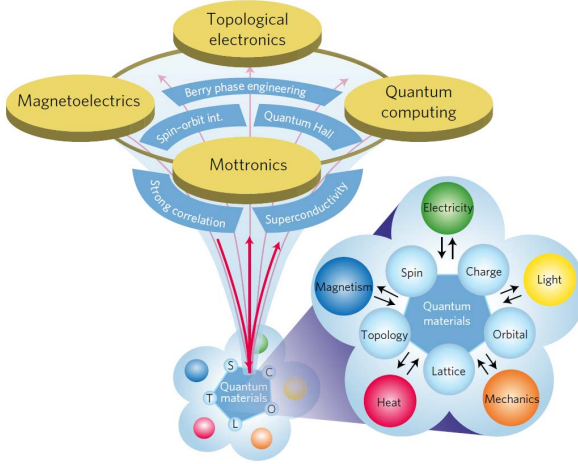


Figure 1.1: **Correlated Materials.** Interplay between the different electronic degrees of freedom and their coupling to external stimuli, resulting in new emergent functions. Adapted from [Tokura et al., 2017].

case of direct bandgap semiconductors; *ii*) the presence of localized magnetic Mie modes originating from the coupling between the high permittivity in the visible range and a suitable nano-engineering of the structure [Shcherbakov et al., 2015, Shcherbakov et al., 2017].

Although both categories (correlated materials and semiconductors/dielectrics) are at the center of a huge research effort, which also helped to unveil intriguing properties, one of the current challenges towards the implementation of high-performance devices consists in the ability to efficiently manipulate and control their functionalities on ultrafast time scales [Shcherbakov et al., 2017, Basov et al., 2017]. In this direction, the excitation by light pulses (typically obtained from ultrafast pulsed lasers) represents a promising control parameter to achieve the control of material properties on-demand. As an example, it has been recently demonstrated by Schiffrin and coworkers [Schiffrin et al., 2013] that the conductivity in a wide-gap insulator (amorphous silicon dioxide) can be increased by many orders of magnitude within 1 femtosecond by the instantaneous light field (few-cycle optical pulse). This result paves the way to electronic signal processing in the petahertz domain, a frequency range not attainable with nowadays electronics [Schiffrin et al., 2013, Basov et al., 2017].

Before providing an overview of the recent achievements in ultrafast manipulation of materials, it is worthy to recall that the properties of photo-excited carriers in solid state systems have been extensively studied in the last decades through time-resolved spectroscopy techniques, in the so-called *pump-probe*

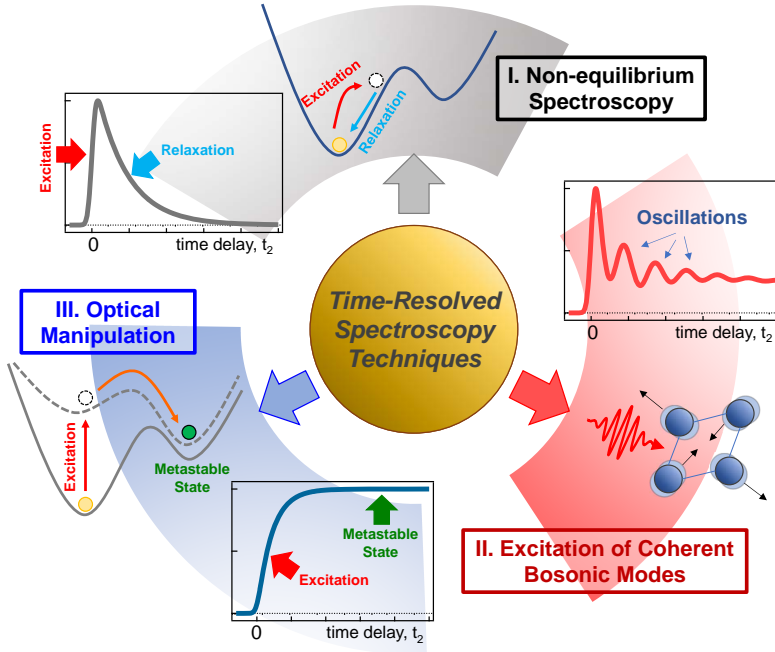


Figure 1.2: **Time-Resolved Spectroscopy Techniques.** Schematic visualization of the three different categories (from [Giannetti et al., 2016]) of time-resolved spectroscopy techniques: (I) Non-equilibrium Spectroscopy, (II) Excitation of Coherent Bosonic Modes, and (III) Optical Manipulation.

configuration. According to this approach, the system under investigation is first driven into an out-of-equilibrium configuration by a strong pulse (*pump*) and its relaxation dynamics is then recorded by a second delayed pulse (*probe*). Time-resolved spectroscopy techniques can be divided into the following categories [Giannetti et al., 2016] (schematically depicted in Fig. 1.2):

- *Non-equilibrium Spectroscopy.* In this case, the system is driven towards a non-equilibrium condition (described by a non-thermal distribution of quasi-particles) by the pump pulse and, then, it relaxes back to equilibrium. By considering the free-energy diagram (schematically reported in Fig. 1.2, sector I), the pump excitation only induces a sudden displacement of the system from the minimum occupied at equilibrium while the shape of the potential is assumed unperturbed. After the excitation, the system relaxes back to its initial configuration, although following a non-thermal pathway. The non-thermal properties which characterize the photo-excited condition are extremely different to those achieved after the

variation of a thermodynamic variable. As a consequence, the relaxation processes in the two cases are different: this represents the advantage of *non-equilibrium spectroscopy*, which goes beyond the simple time-domain approach [Giannetti et al., 2016].

- *Excitation of Coherent Bosonic Modes.* The coupling between the impulsive excitation and a bosonic mode of the system (lattice vibration or charge or spin order) results in a coherent response oscillating at the mode frequency (as sketched in Fig. 1.2, sector II) and decaying with its proper dephasing time. This case represents a time-domain technique since the frequency and lifetime of the mode can be retrieved by Fourier-Transform the signal [Giannetti et al., 2016].
- *Optical Manipulation.* In the case of high-intensity excitations, some systems can be brought very far from the free-energy minimum thus entering regions corresponding to novel non-equilibrium "phases" not accessible through adiabatic transformation. Compared to *non-equilibrium spectroscopy*, in this regime the system does not relax back to the initial configuration, but it reaches a metastable long-living state (see Fig. 1.2, sector III). The resulting overall physical properties of the system originates from the large number of excitations injected on a timescale much faster than the characteristic relaxation time. This is the condition in which photo-induced phase transitions, ultrafast optical switching and the photo-enhancement of superconductivity take place [Giannetti et al., 2016].

Before concluding this section, it is worthy to provide an overview on the typical timescales of the photo-generated carriers in semiconductors. Although this is a specific class of solid state systems, the information which are extracted from time-resolved experiments provides useful and qualitative insights to understand the general mechanisms occurring in other classes of materials. More specifically, we will discuss the case of gallium arsenide (GaAs), which has been intensively studied by pump-probe spectroscopy since the end of the 1980s (see for example [Lin et al., 1987, Schoenlein et al., 1987]). After photo-excitation, the carrier relaxation dynamics evolves according to the following four stages [Weiner, 2009], schematically depicted in Fig. 1.3:

- *Coherent regime (≤ 20 fs)* Within the semiconductor, the pump pulse initially creates excitations whose wavefunctions evolve in phase with the electric field [Sundaram and Mazur, 2002, Weiner, 2009]. This coherence is destroyed by carrier-carrier scattering mechanisms with a characteristic timescale of 200 fs or faster [Weiner, 2009]. In the case of

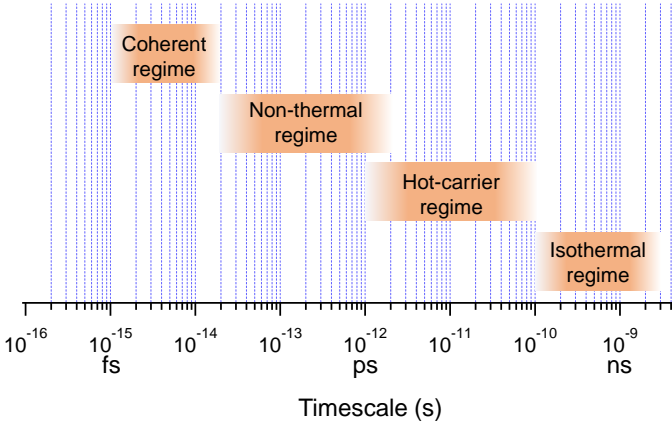


Figure 1.3: **Carrier Relaxation Regimes.** Timescales of photo-excited electronic processes in GaAs (based on [Weiner, 2009]).

GaAs, the dephasing time ranges between 3.5 – 11 fs [Becker et al., 1988, Sundaram and Mazur, 2002].

- *Non-thermal regime* (≤ 2 ps) After the loss of coherence, the excitations (like electron-hole pairs) are left in a non-thermal distribution and they exchange energy among themselves or with the lattice [Weiner, 2009].
- *Hot carrier regime* (≤ 2 –100 ps) After the first preliminary thermalization driven by electron-electron and electron-phonon interactions, the charge carriers are described by a thermal distribution with effective temperatures much higher than the lattice. This is due to the fact that the complete thermal equilibrium with the lattice has not yet been reached. This stage is characterized by the cooling of carrier population through the coupling with high-energy phonon modes of the lattice [Weiner, 2009].
- *Isothermal regime* (≥ 100 ps) After reaching the equilibrium with the lattice, the carriers populations are subjected to radiative and non-radiative recombination processes (in which the energy is released in form of light, through the spontaneous emission of photons, or delivered in other forms than electromagnetic field) leading to the recovery of the initial state [Svelto, 1998, Weiner, 2009].

Starting from this description of the photo-induced out-of-equilibrium properties, we outlined and applied two strategies to induce new functionalities on an ultrafast timescale:

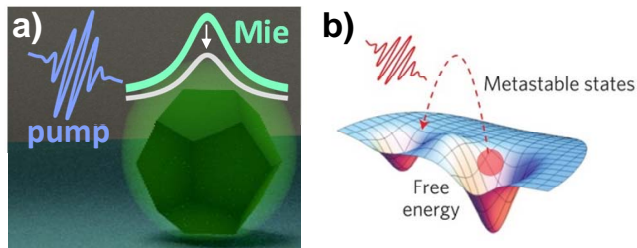


Figure 1.4: **Towards Ultrafast Manipulation** (a) Light excitation can alter the localized Mie modes, thus inducing the nanostructure towards a different (although reversible) interaction with external fields . Adapted from [Franceschini et al., 2020]. (b) By the use of impulsive external stimuli, the system can be driven from the ground state to a new metastable phase. Adapted from [Basov et al., 2017].

- *Coupling between Light and Geometry of Nanostructured Materials.* Within the low-excitation regime, a suitable combination between the geometry of the system (involving the material and its dimensions) and the out-of-equilibrium state can be exploited in high-index dielectric compounds [Makarov et al., 2017b]. In this case, the photo-excited free-carrier injection can be adopted to induce a transient state [Makarov et al., 2017b] of the localized geometry-driven Mie modes (Fig. 1.4a), spectral features corresponding to high concentration of the electromagnetic energy [Mie, 1908]. Specifically, thanks to Fano resonances [Fano, 1961], originating from the interference between the material exciton and the Mie modes in halide perovskites materials [Tiguntseva et al., 2018b], it is possible to control the material optical properties on an ultrafast timescale. This will lead to a versatile platform in which the response to external light fields can be modulated on-demand and in a fast reversible way (this approach will be discussed in Chapter 3).
- *Coherent-Control.* Starting from the possibility to photo-induce a phase transition towards a metastable state (Fig. 1.4b) in correlated materials [Zhang and Averitt, 2014, Basov et al., 2017], the idea consists in applying the coherent-control scheme [Gordon et al., 1999] to vanadium sesquioxide (V_2O_3). Here, the photo-induced insulator-to-metal transition [Liu et al., 2011] is achieved thanks to coherent orbital manipulation, *i.e.* the coherent interaction between light and matter, where the coherence of the electronic degree of freedom represents an additional control parameter to manipulate the phase transition (this approach will be discussed in Chapter 5).

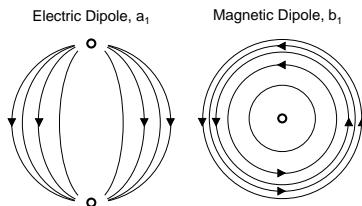


Figure 1.5: **Mie Dipole Modes.** Transverse component of the electric field lines of the electric and magnetic dipole modes. Adapted from [Mie, 1908].

In the following sections, a brief review of some useful reported results towards the implementation of these two strategies will be discussed.

1.2 Coupling between Light and Geometry of Nanostructured Materials

The coupling between light and geometry in nanoscaled materials represents an approach, widely employed in the last decades, towards the realization of (nano)structures endowed by optical properties better performing than those in bulk. After that metals were initially established as the most interesting platform for photonic nanodevices, high-permittivity dielectrics emerged as a valuable alternative due to their lower absorption losses at visible and infra-red frequencies, thus increasing the efficiency of nanodevices [Staude and Schilling, 2017]. Moreover, the recent interest on high-refractive index dielectric materials originated by the observation of electric and magnetic multipolar Mie resonances (named after the theory formulated by Mie, [Mie, 1908]) occurring in nanoparticles at optical frequencies [Staude and Schilling, 2017]. These resonances typically manifest as maxima in the spectra of far-field properties, such as extinction or scattering efficiency. In the case of symmetric shapes (like spheres), the internal and scattered fields can be expressed analytically by a multipolar expansion, where the partial waves of the two fields are coupled [Papoff and Hourahine, 2011, Tzarouchis and Sihvola, 2018]. Moreover, such resonances are particularly appealing from a technological point of view since their resonant excitation (by a suitable external electromagnetic, EM, field) results in a storage of the EM energy within the nanoparticle (which behaves like a resonator) [Evlyukhin et al., 2012], followed by a strong resonant response [Makarov et al., 2017b].

In the case of spherical nanoparticles, the lowest-order resonances correspond to the electric and magnetic dipolar modes (labelled a_1 and b_1 , respectively),

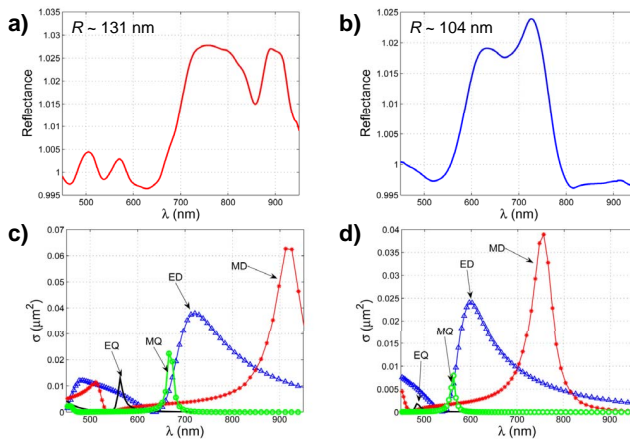


Figure 1.6: **Mie Resonances in Silicon Nanoparticles.** Experimental reflectance spectra for silicon nanoparticles with radii of $R \approx 131$ nm (a) and $R \approx 104$ nm (b). Contribution of the different multipolar modes to the calculated scattering cross section for big (c) and little nanoparticles (d). ED: electric dipole; MD: magnetic dipole; EQ: electric quadrupole; MQ: magnetic quadrupole. Adapted from [Evlyukhin et al., 2012].

schematically displayed in Fig. 1.5. In particular, the latter appears approximately when the condition $\lambda/n = \phi$ is fulfilled, *i.e.* when the value of the wavelength (λ) inside the material (with refractive index n) equals the nanoparticle's diameter (ϕ). This relation provides useful insights under the implementation point of view, stating that the optical response of the nanosphere can be tailored by a suitable design of the geometry [Staude and Schilling, 2017]. In particular, in high-index nanoresonators, magnetic dipolar resonances attract a lot of attention since their excitation is due to the electric component of the external field and not by the magnetic one. Moreover, the higher quality factor (Q -factor) exhibited by low-order magnetic multipoles determines a higher enhancement of the electric field inside the nanostructure, compared to the corresponding electric modes [Makarov et al., 2017b].

One of the first successful experimental observations of magnetic and electric resonances (corresponding to dipolar modes) in the visible spectral range was made by Evlyukhin and coworkers for spherical silicon nanoparticles with diameters of ~ 200 nm [Evlyukhin et al., 2012, Staude and Schilling, 2017]. The choice of silicon as constituent material for the implementation of dielectric nanostructures is due to several reasons: high refractive index (*e.g.*, at $\lambda = 800$ nm, $n = 3.694$ and $k = 0.007$, [Aspnes and Studna, 1983]), low absorption losses, high nonlinear properties, low cost and mature (nano)fabrication technology, and good compatibility with complementary

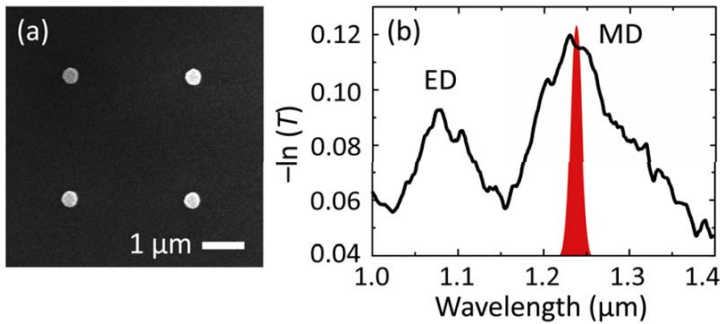


Figure 1.7: **Third-Harmonic Generation in Silicon Nanodisks.** (a) SEM image of a periodic lattice of silicon nanodisks. Diameter= 360 nm, height= 260 nm, and period= 2.85 μm . (b) Transmission spectrum of the sample (black solid line). The red area represents the pump pulse spectrum adopted for the third-harmonic generation. ED: electric dipole; MD: magnetic dipole. Adapted from [Shcherbakov et al., 2014].

metal-oxide-semiconductor (CMOS) technology [Staude and Schilling, 2017, Makarov et al., 2017b]. In their experiment, Evlyukhin and coworkers employed spatially resolved linear reflection spectroscopy to investigate the scattering properties of silicon nanoparticles with different sizes. In particular, Fig. 1.6 displays the experimental reflection spectra measured for silicon nanoparticles with radii of $R \approx 131$ nm and $R \approx 104$ nm (panels a and b, respectively). The complex shape of the spectra originates from the contribution of the different multipole modes (Figs. 1.6c and d) to the total scattering cross-section. As suggested from the modes decomposition, magnetic dipole and electric dipole moments represents the first two resonances at high wavelength (low frequency) and they dominate the scattering properties in the visible part of the spectrum [Evlyukhin et al., 2012]. In addition, the red-shift of the resonances position for bigger nanoparticles (in line with the previous observation of the relationship between the spectral position of the magnetic dipole mode and the nanoparticle size) explains the spectral shift of the reflectance spectra. Therefore, this experiment, besides being among the first observation of strong light scattering by individual high-permittivity nanospheres, demonstrates that the optical properties of a nanostructure can be tailored thanks to a suitable tuning of the geometry [Evlyukhin et al., 2012].

The capability of nanostructures (and metamaterials) to efficiently storing the electromagnetic energy, giving rise to a strong confinement, represents a powerful tool to activate new optical properties both at- and out-of-equilibrium. In the former case, for example, this feature has been exploited to achieve an efficient third harmonic signal in silicon nanodisks (see Fig. 1.7a), which is two-order of

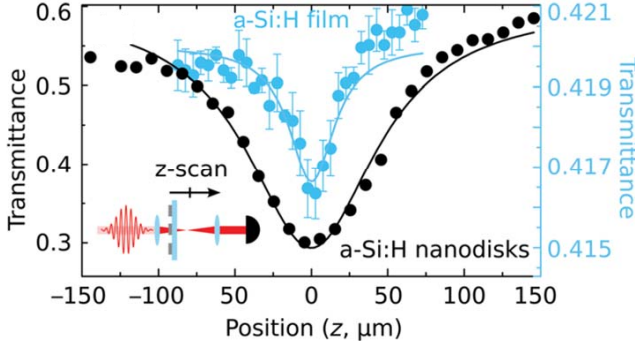


Figure 1.8: **Two-photon Absorption Enhancement in Silicon Nanodisks.** z -scan measurement of the resonant nanoparticles (black markers) and of the amorphous film (blue markers). The solid lines represent the fitting curves providing a value of 5.6 (0.7) cm/kW for the TPA coefficient for the nanodisks (film). The spectrum of the laser is centered at 780 nm. The film thickness equals the height of the nanodisks (130 nm). Adapted from [Shcherbakov et al., 2015].

magnitude higher than in the counterpart bulk form [Shcherbakov et al., 2014]. In this experiment by Shcherbakov and coworkers, the enhanced third-harmonic (3ω) signal was generated from a fundamental (ω) pump pulse, whose spectrum is carefully tuned in order to resonantly excite the magnetic dipole mode of the nanodisk (see Fig. 1.7b). The strong confinement of the electromagnetic energy, giving rise to the geometrical resonance of the nanodisk, strongly influences its optical properties [Shcherbakov et al., 2014].

Another interesting example where nonlinear properties are significantly enhanced by the use of resonant dielectric nanospheres is given by the experiment by Shcherbakov and coworkers, where they demonstrated that the effective value of the two-photon absorption (TPA) coefficient for an array of silicon nanodisks can be increased by almost two orders of magnitude with respect to that of a bulk amorphous film [Shcherbakov et al., 2015, Makarov et al., 2017b]. As shown in the z -scan measurement in Fig. 1.8, the transmittance of the array of silicon nanodisks is characterized by a drop, near the laser focus position, whose amplitude is two order of magnitude higher than in the case of the amorphous silicon film. The Mie resonance induced enhancement is confirmed by the value of the TPA coefficient, which is estimated 5.6 cm/kW (0.7 cm/kW) in the case of the array of nanodisks (amorphous film) [Shcherbakov et al., 2015, Makarov et al., 2017b].

The enhancement of nonlinear properties in resonant dielectric nanoparticles resulting from the strong field confinement represents also an important tool to achieve optically tunable functionalities on an ultrafast time

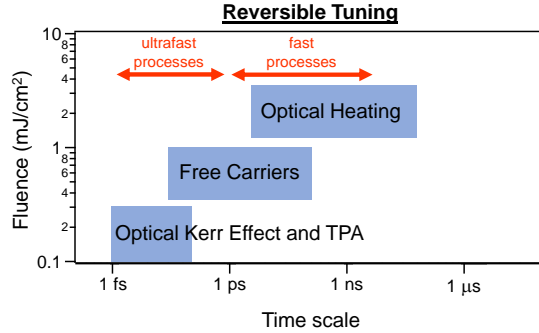


Figure 1.9: **Reversible Tuning.** Schematic diagram of laser-induced tuning mechanisms. TPA: two-photon absorption. Adapted from [Makarov et al., 2017b].

scale, like optical modulation or ultrafast switch [Shcherbakov et al., 2015, Makarov et al., 2017b]. Typically, the tuning of nanostructures and metasurfaces is accomplished by *fast reversible* or *permanent non-reversible* processes [Makarov et al., 2017b]. For our purposes, I will focus on the first approach, where a laser excitation is employed to change the material permittivity [Makarov et al., 2017b], thus reaching an out-of-equilibrium state which eventually relaxes back to equilibrium.

In the following, the term *switch* will refer to the whole cycle involving both excitation and relaxation processes. In order to achieve an ultrafast switch, the first important aspect to take into account is the time-duration of laser pulses adopted to photo-induce the out-of-equilibrium state. Indeed, in the case of an instantaneous process, the time duration of the switch equals the pulse duration [Shcherbakov et al., 2015]. Therefore, to achieve ultrafast switching, ultrashort pulses (with few tens of femtoseconds pulse duration) should be employed. Furthermore, the other important aspect is related to the relaxation time of the mechanism inducing the permittivity variation [Makarov et al., 2017b]. The reversible modulation of the material properties can be accomplished, for example, by nonlinear processes involving charge carriers, whose typical time scales were introduced in Sec.1.1. Due to laser irradiation, the ultrafast injection of *free carriers* causes a variation of the refractive index by varying the plasma frequency. Then, their relaxation (ranging from 1 – 100 ps) is responsible for another modulation process, *optical heating*, in which the variation of permittivity is due to the increase of the lattice temperature resulting from electron-phonon scattering. However, as highlighted by the diagram in Fig. 1.9, these two mechanisms relax on the picosecond or nanosecond time scale (in the case of optical heating, the relaxation through phonon-phonon scattering lies in the range of 1 – 100 ns). Therefore, in order to achieve an ultrafast relaxation, all-

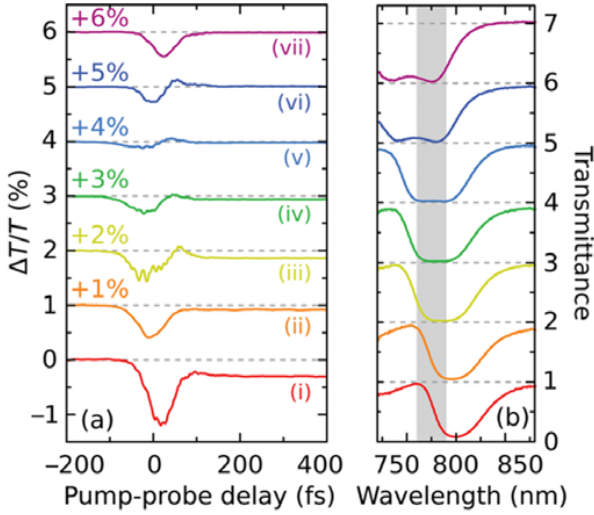


Figure 1.10: **Ultrafast Switching in Silicon Nanodisks.** (a) Time-resolved transient transmittance for seven different samples (the diameter size increases from top to bottom), whose equilibrium transmittance is reported in (b). The gray area denotes the spectral region (FWHM) occupied by the 45-fs pump pulse adopted in the experiment ($30 \mu\text{J}/\text{cm}^2$ fluence). Adapted from [Shcherbakov et al., 2015].

optical nonlinear processes should be addressed. In these cases, the modulation of the material refractive index can be induced by *Kerr nonlinearities*, the analog of the traditional Kerr electro-optical effect, or two-photon absorption. For these mechanisms, the modulation of the optical response relaxes on an ultrafast time scale (< 100 fs) [Makarov et al., 2017b].

The possibility to achieve ultrafast all-optical switching in dielectric nanostructures was first demonstrated by Shcherbakov and coworkers thanks to a time-resolved pump-probe experiments on amorphous silicon nanodisks with different diameters in the range between 210 – 280 nm in order to ensure the spectral overlap between the magnetic resonance and the 45-fs pump pulse employed [Shcherbakov et al., 2015]. As reported in Fig. 1.10a, the time-resolved transient transmittance ($\Delta T/T$) curves exhibit a pulse-limited spike at zero delay followed by a finite post-pulse tail for bigger nanodisks. The former feature is due to two-photon absorption (TPA) process, while the latter is ascribed to free-carrier relaxation (with a typical timescale of ~ 30 ps for these samples) [Shcherbakov et al., 2015]. Clearly, the transmission of the probe pulse through the metasurface is modulated by pump excitation, which resonantly triggers the magnetic modes of the nanodisks and, for some nanodisk dimension, injects free-carriers. Interestingly, as suggested in the case of samples (v)-(vii),

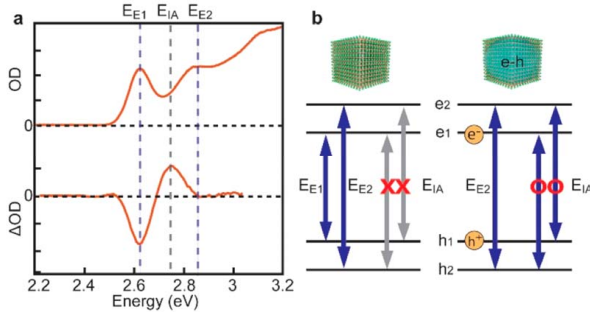


Figure 1.11: **Light-induced Switching in Perovskite Quantum Dots.** (a) At- and out-of-equilibrium absorption spectra, at 10 ps time delay, (top and bottom, respectively) for CsPbBr₃ quantum dots with size of 4.1 nm. The dashed lines denote the first and second exciton transition (E_{E1} and E_{E2}) and the induced absorption (E_{IA}). (b) Schematic diagram of the at- and out-of-equilibrium transitions (left and right, respectively) pairing electron and hole states with different and same parity, respectively. Confined electron (hole) levels are denoted by e_1 and e_2 (h_1 and h_2). Adapted from [Rossi et al., 2018].

when the pump spectrum is tuned towards the right slope of the magnetic resonance (dip in the transmission) as shown in Fig. 1.10b, the contribution of the free-carriers vanishes and only the TPA-induced spike (whose width is 65 fs) remains. In this condition, an all-optical switching of the metasurface is achieved on the ultrafast timescale [Shcherbakov et al., 2015].

This experiment highlights the role of geometry tuning towards the activation of transient new functionalities in materials. On one side, thanks to the coupling with the strong confined optical modes, it gives rise to a strong enhancement of nonlinear processes with respect to bulk (in this case, two-photon absorption is magnified by a factor of 80, [Shcherbakov et al., 2015]). On the other hand, it represents a useful control knob to suppress undesirable effects (in this case, the free-carrier relaxation processes which would increase the total recovery time).

In the example presented before, the tuning of the geometry of the material has been performed up to an intermediate level. Indeed, starting from the bulk form, previous examples considered structure with a characteristic size of the order of the wavelength in the visible. Going further in this direction, thus reaching an extreme lowering of the material size, leads to a strong interaction between the charge carriers and the lattice [Rossi et al., 2018], thus enabling new functionalities in combination with a suitable light excitation. Recently, perovskite quantum dots (QDs) exhibited the activation of a formally forbidden transition in the photo-induced out-of-equilibrium regime [Rossi et al., 2018].

In their experiment, Rossi and coworkers investigated the out-of-equilibrium

spectral and temporal dynamics of perovskite CsPbBr₃ QDs of different sizes (between 3.7 and 6.9 nm), photo-excited in a low-density regime ($\sim 3.5 \mu\text{J}/\text{cm}^2$) [Rossi et al., 2018]. As shown in Fig. 1.11a in the case of 4.1-nm size QDs, compared to the equilibrium absorption spectrum (top), showing two peaks ascribed to the first (E_{E1}) and second (E_{E2}) exciton transitions, which pair electron and hole states with different parity, the out-of-equilibrium spectral signal at 10 ps time delay (bottom) reveals the presence of a induced absorption feature at an energy E_{IA} , located between E_{E1} and E_{E2} and activated on a sub-picosecond time scale (850 fs for 3.7-nm size QDs) [Rossi et al., 2018]. Their analysis demonstrates that the photo-induced absorption feature corresponds to a transition pairing electron and hole states with the same parity (blue arrows with red markers in Fig. 1.11b) and that the modification of the optical selection rule is a consequence of the interaction between the lattice and the strong quantum confinement of the exciton. Indeed, when the pump pulse triggers the carriers, an exciton is initially excited. Due to the strong confinement, the exciton induces the formation of electron and hole polarons in spatially different locations of the lattice. The strong perturbation is capable to modify the selection rule for the exciton transition thus allowing the spectral feature at E_{IA} [Rossi et al., 2018]. This experiment demonstrates that light represents a powerful tool to induce transient functionalities on an ultrafast time-scale (also in combination to some "cascade" mechanisms), thus allowing the observation of new optical properties different from those at equilibrium.

1.3 Coherent Control

The approach towards the coherent manipulation of the electronic properties of materials belongs to a wider approach aiming at controlling the electronic properties by exploiting the the intrinsic coherence of the light-matter interaction on time scales faster than the coupling of electrons with other degrees of freedom (decoherence). Within this framework, the development of narrow-band lasers triggered first the development of new methods to control the output (*i.e.*, yield and product distribution) of chemical reactions, which mainly involve atomic or molecular systems. Indeed, compared to previous protocols in which the thermodynamics variables (temperature and pressure) represented the reaction control parameter, laser sources provided a new tool in this direction: the phase properties of the electromagnetic field can be used to control the output of a reaction. This led to the development of photochemical methods, labelled as *coherent control*, which exploits the phase in order to manipulate the reaction pathways [Gordon et al., 1999]. In this context, therefore, the choice of atomic and molecular systems as the first platform for the implementation of coherent

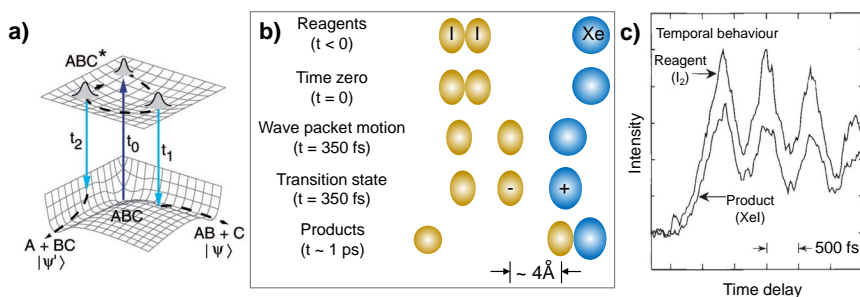


Figure 1.12: **Coherent Control: Time Domain Approach.** (a) Sketch of the Tannor-Rice scheme. At time t_0 an ultrafast pulse (excitation, dark blue upward arrow) creates a wave packet, which then evolve freely during time. According to the time delay (t_1 or t_2), a second pulse (dump, light blue downward arrow) transfers the population into different product channels ($AB+C$ or $A+BC$, respectively). Adapted from [Nuernberger et al., 2007]. (b) Sketch of the reaction $Xe+I_2 \rightarrow XeI+I$ at different delay times. Adapted from [Potter et al., 1992]. (c) Yield product of XeI as function of the time delay between the two laser pulses. Adapted from [Potter et al., 1992].

control experiments is related to their long-lasting coherent regime, whose time scale can be up to few tens of nanoseconds [Jain et al., 1996].

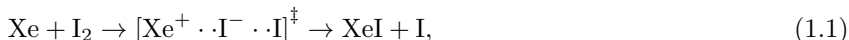
In this framework, two schemes have attracted particular interest and they are based on two different properties of the laser radiation [Gordon et al., 1999]. In the first method, initially proposed by Tannor and Rice, the control parameter is given by the temporal delay between two coherent laser pulses, labelled *excitation* and *dump* [Tannor and Rice, 1985]. According to this time-domain method [Nuernberger et al., 2007], the first ultrafast pulse (excitation) creates a coherent superposition of eigenstates (*wave packet*) in the system under treatment ($ABC \rightarrow ABC^*$ at $t = 0$ in Fig. 1.12a). According to the degree of freedom addressed, the wave packet can be vibrational or electronic in nature. Given its non-stationary behaviour, the wave packet evolves during time and it passes through different configurations. When the system reaches the configuration corresponding to some outcome, the second pulse (dump) transfers the population to the product state. Since during the free temporal evolution the system assumes different configurations, by carefully tuning the time delay between the excitation and dump pulse various reaction outcomes can be accessed (*e.g.*, $AB+C$ at t_1 or $A+BC$ at t_2 , as depicted in Fig. 1.12a) [Gordon et al., 1999, Nuernberger et al., 2007].

Experimentally, this method was adopted by Potter and coworkers to control, on a femtosecond timescale, the yield of product XeI in the reaction between

Table 1.1: **Coherence Time Values.** Comparison between coherence time values for different systems.

Description	T_2 value	Reference
Atomic coherence on a Raman transition in Pb vapor	14 – 28 ns	[Jain et al., 1996]
Vibrational coherence associated to a torsional mode in stilbene ($C_{14}H_{12}$)	~ 100 fs	[Szarka et al., 1995]
Molecular vibration in molecular I_2 in solid Kr	34 – 110 ps	[Karavitis and Apkarian, 2004]

iodine molecules and Xe atoms:



thanks to light-assisted nuclear vibrational motion [Potter et al., 1992]. In particular, as sketched in Fig. 1.12b, the first laser pulse (pump) induces an intermediate state (wave packet) for the iodine molecule, in which the atoms oscillate around their equilibrium distance with a well defined period. Thanks to electron transfer, the Xe atom *harpoons* iodine thus to reach a transition state. Finally, the second pulse (dump), delayed with respect to the first one by means of a Michelson interferometer, allows the transition to occur by providing to the wave packet the necessary energy to overcome the reaction threshold. As depicted in Fig. 1.12c, by carefully tuning the delay between the two laser pulses, the yield product of XeI can be maximized [Potter et al., 1992]. This work demonstrates that the ultrafast manipulation of the vibrational coherence, *i.e.* the coherent motion of the wave packet along the chemical bond coordinate, represents the key element to achieve the "switch" control effect in the chemical reaction [Potter et al., 1992]. At this stage, it must be emphasized that the coherent dynamics of the reaction can be controlled by a coherent external excitation as long as the quantum system under manipulation does not interact with its surrounding environment. Indeed, intra- and intermolecular reactions characterizing condensed systems significantly shorten their coherence time (T_2) with respect to isolated systems, like gas phases (see Tab. 1.1 for a comparison of the coherence time values) [Nuernberger et al., 2007].

The second method exploits the relative phase between two excitation pulses as the control parameter. In this energy-domain method, initially proposed by Brumer and Shapiro [Brumer and Shapiro, 1986], the system is triggered

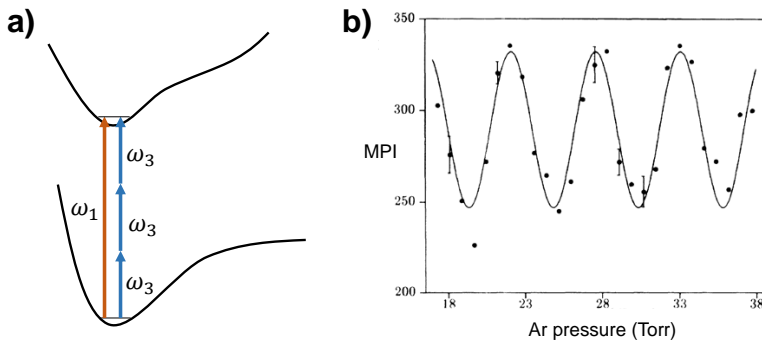


Figure 1.13: **Coherent Control: Energy Domain Approach.** (a) Schetch of the Brumer-Shapiro scheme. In presence of both laser beams, the transition from the initial to the final state can occur by the absorption of either one or three photons ($n = 1$ and $m = 3$). Adapted from [Gordon et al., 1999]. (b) Ionization signal of atomic mercury as a function of the Argon pressure inside the reaction chamber. Adapted from [Chen et al., 1990].

simultaneously by two laser pulses, set at two different frequencies (ω_m and ω_n). Moreover, this method takes advantage on the fact that the system, in order achieve the final state from the initial one, can follow two competing paths: the first involves the absorption of m photons at frequency ω_m , while the second requires n photons at frequency ω_n (as shown in Fig. 1.13a); therefore, the following relation must hold between the laser frequencies: $m\omega_m = n\omega_n$ [Gordon et al., 1999]. The control of the final state population (*i.e.* the branching ratio of the reaction) is achieved by carefully tuning the relative phase between the two beams. Analogously to the double-slit experiment, in which the interference between the two pathways gives rise to an interference pattern, in this method the interaction involves the matrix elements of the operators which connect the initial state to the final one [Gordon et al., 1999, Nuernberger et al., 2007].

One of the first successful applications of this method to atomic systems was performed by Chen and coworkers. In this experiment, they considered the $6s\ ^1S_0 \rightarrow 6p\ ^1P_1$ transition in mercury excited by two laser beams at different frequencies. The interference between the linear and non-linear excitation pathways is tuned by changing the phase between the two fields and gives rise to a modulation of the ionization probability of atomic mercury, as shown in Fig. 1.13b. In their apparatus, phase shift is accomplished by changing the Argon pressure in the chamber where the reaction takes place. Indeed, since the fields have different central wavelength, their propagation in the reaction chamber is described with different refractive indexes. Therefore, a variation in the pressure inside the chamber results in a modulation of the relative phase

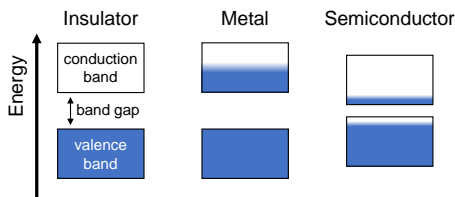


Figure 1.14: **Band Structure.** Schematic band occupancy for an insulator, metal, and semiconductor. Adapted from [Kittel, 2005].

[Chen et al., 1990].

The possibility to transfer the concept of active optical control from molecules to solids is not straightforward, since the latter systems are characterized by high electronic and vibrational density of states, which hinder the preservation of coherent excitation on longer time scales [Horstmann et al., 2020]. Regarding solids, one of the most remarkable descriptions of the electronic states in these systems was developed by Bloch [Bloch, 1929] within the independent electron approximation. In this picture, the periodicity of the crystal lattice determines the properties of the electronic levels [Ashcroft and Mermin, 1976], which consists in energy bands arising from the overlap between atomic orbitals. These bands are separated by forbidden regions (called *band gaps*), in which no available states exist [Kittel, 2005], see Fig. 1.14. When the allowed energy bands are completely filled, the solid behaves like a band insulator [Imada et al., 1998]. In this case, the highest occupied band is called valence band, while the lowest unoccupied one is labelled as conduction band. On the other hand, when the (conduction) band is partially filled, the system behaves like a metal [Kittel, 2005]. In addition to these, semiconductors constitute a class of system which are insulating at $T = 0$, but the size of their energy gap² (between the valence and conduction bands) is such that thermal excitations give rise to an observable conductivity at room temperature [Ashcroft and Mermin, 1976].

In this context, crystalline system (in particular, semiconductors) represents a better platform, compared to atoms or molecules, to launch a coherent current flow thanks to a proper excitation of carriers through the bandgap [Tsen, 2001]. Indeed, in these system, the photo-generation of current is not subjected to state selectivity (typical constraint in atoms and molecules), which implies the choice of discrete initial and/or final states, thus it originates from the contribution of all Bloch states in the conduction and valence bands [Tsen, 2001]. This is the key point exploited by Haché and coworkers who theoretically [Atanasov et al., 1996]

²For semiconductors, the value of the energy gap ranges from tenths up to few eV [Ashcroft and Mermin, 1976].

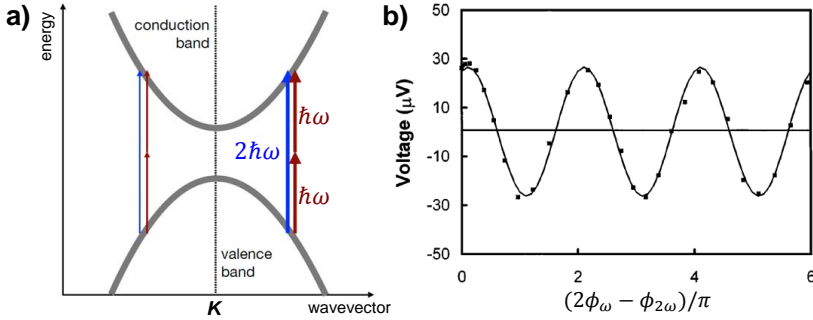


Figure 1.15: **Coherent Control of Photo-current in GaAs.** (a) The interference between the direct absorption process at 2ω (blue upward arrow) and the two-photon process at ω (red upward arrow) gives rise to an excitation asymmetry at momenta $\mathbf{K} + \mathbf{k}$ and $\mathbf{K} - \mathbf{k}$, where \mathbf{K} is a generic high-symmetry wavevector of the crystal. The relative phase of the 2ω and ω fields regulates the direction of the excitation asymmetry. Adapted from [Ronchi et al., 2018]. (b) Photo-induced coherent current as a function of the relative phase between the two excitation beams. A sine function (solid curve) is fitted to the experimental data (markers). The device under test consists in a metallic-semiconductor-metallic structure, with two gold electrodes ($5 \mu\text{m}$ gap) deposited on the GaAs layer. Adapted from [Haché et al., 1997].

and experimentally [Haché et al., 1997] demonstrated the coherent generation and control of photo-current in bulk semiconductor GaAs.

In their *energy-domain* coherent control experiment, two phase-related excitations (at ω and 2ω) couple valence and conduction band states, across the band gap (E_g), with same energies but different wave vectors, as shown in Fig. 1.15a [Haché et al., 1997]. The energy difference between the Bloch semiconducting states is determined by the photon energy of the fundamental excitation, which satisfies the relation $E_g/2 < \hbar\omega < E_g$ [Atanasov et al., 1996]. Upon photo-excitation, the interference between the two different quantum pathways (single- and two-photon-absorption processes) causes an anisotropic polar distribution of carriers in \mathbf{k} space [Haché et al., 1997]. Therefore, a macroscopic current is generated, whose amplitude and direction can be manipulated by a proper tuning of the relative phase of the two beams: $\Delta\phi = 2\phi_\omega - \phi_{2\omega}$, where ϕ_ω ($\phi_{2\omega}$) is the phase of the field amplitude at ω (2ω), as shown in Fig. 1.15b [Haché et al., 1997]. In experiment on GaAs, the tuning of $\Delta\phi$ is accomplished by rotating a BK7 glass window, which varies the optical path of the two collinearly propagating beams at 0.775 (2ω) and $1.55 \mu\text{m}$ (ω) [Haché et al., 1997].

In order to better understand the mechanism behind this coherent control protocol, it is instructive to calculate the carrier injection rate (or orbital polarization) in a simple two-band model (v : valence band; c : conduction band)

by means of time-dependent perturbation theory. The states of interest are the ground (initial) state $|0\rangle$ and states of the form $|cv, \mathbf{k}\rangle = a_{c\mathbf{k}}^\dagger b_{v\mathbf{k}}^\dagger |0\rangle$, where $a_{c\mathbf{k}}^\dagger$ ($b_{v\mathbf{k}}^\dagger$) creates an electron (hole) at wave vector \mathbf{k} in the conduction (valence) bands. In the presence of a perturbation given by a classical electromagnetic field (which is composed by two fields at frequencies ω and 2ω), the state describing the system at time t can be developed as $|\Psi(t)\rangle = c_0(t)|0\rangle + c_{cv, \mathbf{k}}(t)|cv, \mathbf{k}\rangle$. Starting from the Fermi's golden rule, the carrier density injection rate takes the form:

$$\dot{n} = \frac{2}{V} \sum_{\mathbf{k}} \frac{d}{dt} |c_{cv, \mathbf{k}}|^2 = \frac{4\pi}{V} \sum_{\mathbf{k}} |K_{cv, \mathbf{k}}|^2 \delta(\omega_{cv}(\mathbf{k}) - 2\omega), \quad (1.2)$$

where V is the normalization volume of the crystal and $\omega_{cv}(\mathbf{k}) = \omega_c(\mathbf{k}) - \omega_v(\mathbf{k})$, with $\omega_c(\mathbf{k})$ and $\omega_v(\mathbf{k})$ representing the dispersion relations of the conduction and valence band, respectively. In this formulation, the matrix element $|K_{cv, \mathbf{k}}|^2$ reads:

$$\begin{aligned} |K_{cv, \mathbf{k}}|^2 = & \hat{\zeta}_{1, cv}^{ab}(\mathbf{k}) E^a(-2\omega) E^b(2\omega) \\ & + \hat{\zeta}_{2, cv}^{abcd}(\mathbf{k}) E^a(-\omega) E^b(-\omega) E^c(\omega) E^d(\omega) \\ & + \left[\hat{\zeta}_{3, cv}^{abc}(\mathbf{k}) E^a(-\omega) E^b(-\omega) E^c(2\omega) + c.c. \right], \end{aligned} \quad (1.3)$$

where superscripts indicate Cartesian components (to be summed over if repeated), $E(\omega)$ and $E(2\omega)$ are the electric field amplitudes at the indicated frequencies and $\hat{\zeta}_1$, $\hat{\zeta}_2$ and $\hat{\zeta}_3$ are second-, fourth-, and third-rank tensors. The three different terms of the right-hand side of Eq. 1.3 represent: 1) the pure one-photon contribution; 2) the pure two-photon contribution; 3) the interference between the two-photon and one-photon transition processes. While $\hat{\zeta}_1$ and $\hat{\zeta}_2$ are even under the symmetry operation $+\mathbf{k} \rightarrow -\mathbf{k}$ with respect to a high-symmetry wave vector, the $\hat{\zeta}_3$ is odd under the same operation and is thus responsible for the asymmetric distribution of the injected carriers around the high-symmetry point [Tsen, 2001, Ronchi et al., 2018].

Although this experiment represents an important achievement regarding an effective application of coherent control of an electric current on a sub-picosecond timescale in a solid state system [Schiffrin et al., 2013], the key role is played by the coherence of the light excitation, while that belonging to one of the degrees of freedom of the system under investigation little contributes.

Regarding the possibility to exploit the vibrational or electronic coherence in a *time-domain* coherent-control experiment in solid state systems, as suggested

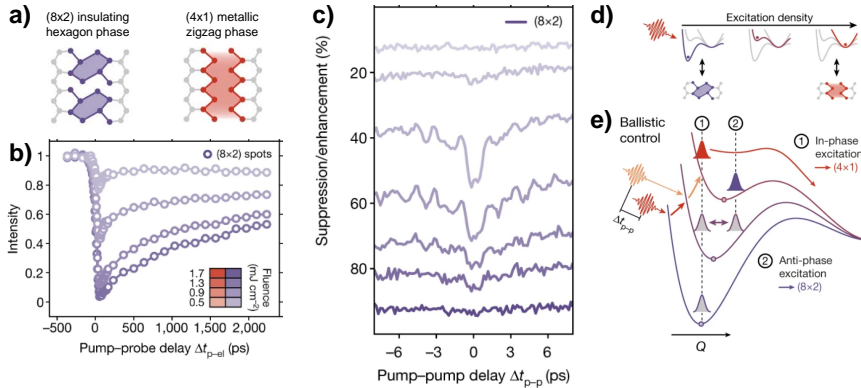


Figure 1.16: **Coherent Control Scheme in Low-Dimensional Materials.** (a) Structure of atomic indium wire on the Si(111) surface. Left (right): below (above) T_c . (b) Time-dependent integrated intensity of the (8×2) diffraction spots for different fluences. (c) Intensity of the (8×2) diffraction spots as a function of the time delay between the two pump pulses for different excitation levels. (d) Tristable potential diagram for the single pulse excitation. (e) Coherent control mechanism for the double-pulse excitation scheme: in-phase (1) and anti-phase (2) excitation. Adapted from [Horstmann et al., 2020].

by Horstmann and coworkers, low-dimensional systems represent promising candidates since the typical phase transitions exhibited by these materials can be thought as *reactions* (similar to the chemical ones) and can be induced by different mechanisms: photo-induced transient heating, electronic excitation, or direct coupling to vibrational modes [Horstmann et al., 2020].

In this direction, Horstmann and coworkers recently demonstrated the coherent control over a metal-insulator structural phase transition in atomic indium wires deposited on the (111) surface of silicon. This quasi-one-dimensional solid-state system, arranged in a zigzag pattern, exhibits a metallic (4×1) phase at room temperature, which turns into an insulating (8×2) state below a critical temperature ($T_c = 125$ K), as shown in Fig. 1.16a. In this material, the phase transition from the insulating to a ns-living metallic metastable (4×1) state can be induced upon photo-excitation, as shown in Fig. 1.16b. Here, the time dependence of the intensity of the (8×2) diffraction spots is displayed for a time resolved experiment in which the system is photo-excited by an optical pump and the structural properties are detected thanks to an ultrafast low-energy electron diffraction (ULEED) probe. However, when the system is triggered by a double-pulse excitation scheme, the ULEED signal (recorded as a function of the delay between the two pump pulses at fixed probe delay time) exhibits oscillations with period of 1 – 2 ps, as displayed in Fig. 1.16c. The frequencies of these oscillations correspond to shear and

rotational phonon modes identified as amplitude modes (coherent oscillations of the periodic lattice distortion) of the phase transition. Moreover, this oscillating pattern demonstrates a coherent response to photo-excitation, meaning that the switching efficiency controlled by the second pulse is determined by the coherent vibrational motion imposed by the first one (similar to the molecular case previously presented). In order to better understand this aspect, it is worthy to briefly recall the description of the $(8 \times 2) \rightarrow (4 \times 1)$ transformation and discuss the mechanisms involving vibrational modes along the reaction coordinate (amplitude modes). In particular, the $(8 \times 2) \rightarrow (4 \times 1)$ transition is treated thanks to a potential profile with three minimum positions. At the very beginning, the system is in the position corresponding to the (8×2) configuration. In the case of a single pulse, the system is pushed towards the (4×1) by the electronic excitation (see Fig. 1.16d), but displacive excitation of coherent phonons (DECP) also occurs and its effect plays a crucial role in the double-excitation scheme. Indeed, while the DECP effect is maximized in the case of in-phase excitation, thus allowing the system to cross the barrier and reach (4×1) configuration (path 1 in Fig. 1.16e), on the other hand, this contribution is damped for anti-phase excitation, thus the system remains trapped in the (8×2) configuration (path 2 in Fig. 1.16e). Therefore, the manipulation of the phonon coherence represents a powerful tool to control the phase-transition on-demand [Horstmann et al., 2020].

In addition to low-dimensional systems, Horstmann and coworkers suggested that also correlated materials represents a good platform in which coherences can be exploited to affect the transition [Horstmann et al., 2020]. However, in these compounds, the coherence which would couple to the photo-induced phase transition is the electronic one. At this stage it is worthy to underline that the study of the (electronic) polarization dynamics in *time-domain* coherent control experiments at optical frequencies (typical for the system under investigation) has to cope with both experimental challenges and the nature of the electronic excitation itself [Tollerud and Davis, 2017]. Regarding the first aspect, conventional detectors and electronics are not capable to measure the time evolution of electric fields (of the signal) at optical frequencies (300 – 700 THz, with optical period of the order of 1.4 – 3.3 fs). To overcome this limitation, an interferometric approach is usually employed [Tollerud and Davis, 2017]. In turn, in order to correctly interpret the results, this protocol requires a high-level control of the phase stability between the pulses since the phase of the signal reflects the phase of the excitation pulses [Tollerud and Davis, 2017].

On the other hand, the time scale of the polarization dynamics sets the limits for the temporal duration of the pulse adopted in the experiment. In the case of condensed phase systems, the electronic coherence time ranges from

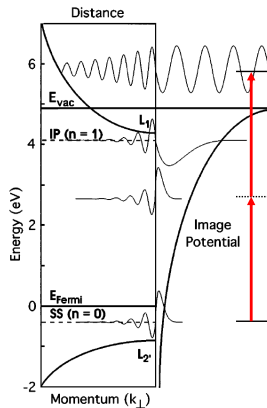


Figure 1.17: **Interferometric Two-Photon Time-Resolved Photoemission.** Sketch of the two-photon (red upward arrows) photoemission process, which starts from the surface state (SS), proceeds through a virtual state (located at 1.4 eV below the $n = 1$ image potential, IP, state), and ends in an outgoing free-electron wave. Adapted from [Ogawa et al., 1997].

few femtoseconds to hundreds of picoseconds. In particular, in the case of materials exhibiting insulator-to-metal transition, such as Mott insulators, the coherence time is of the order of 2 – 6 fs [Gandolfi et al., 2017]. Therefore, a pulse width of the order of 10 fs is required to resolve these dynamics [Collini, 2013, Tollerud and Davis, 2017].

In solid state systems, one of the first examples of coherent control of electron dynamics is represented by the works from Ogawa, Petek, and coworkers on metal surfaces [Petek and Ogawa, 1997, Ogawa et al., 1997, Petek et al., 1997]. In their experiments, two phase-locked pump pulses are adopted to induce transitions between electronic bands with appropriate symmetry thus inducing the photoemission of electrons from the occupied surface state in Cu(111), see Fig. 1.17, according to an interferometric two-photon process [Ogawa et al., 1997, Petek et al., 1997]. Compared to traditional absorption and reflection techniques (which provides the total electronic response) [Ogawa et al., 1997], this approach allowed Ogawa and coworkers to measure energy-, momentum-, and phase-resolved polarization dynamics at metal surface, thus demonstrating that the photoemission spectra (*i.e.* electron distribution) depends on the phase between the optically coherent excitations [Ogawa et al., 1997, Petek et al., 1997]. Under an experimental point of view, the control of the coherent polarization dynamics has been made possible by adopting: *i*) ultrashort laser pulses endowed by a temporal duration (~ 15 fs) slightly shorter than the dephasing time ascribed to the electronic transition under study (~ 20 fs) and *ii*) high-level control (sub-

femtosecond resolution) of the interferometric scanning between the pump pulses, generated by a Mach-Zender interferometer [Ogawa et al., 1997]. In addition to metals [Petek and Ogawa, 1997], the interferometric two-photon scheme has been adopted also to study the coherence properties of electron-hole pairs in a high- T_c superconductor as $\text{Bi}_2\text{Sr}_2\text{CaCu}_2\text{O}_{2+\delta}$ [Nessler et al., 1998b, Nessler et al., 1998a]. More recently, a multi-photon approach has been developed for coherent multidimensional photoelectron spectroscopy of metal surfaces [Reutzel et al., 2019].

This experiment provides useful insights on the technical details towards the coherent manipulation of the electronic coherence in solid state materials. In our case, we will exploit this as an additional control parameter in the photo-induced phase transition in correlated materials. In particular, our attention will focus on Mott insulators. Therefore, the next section will provide a description of the electronic properties of these compounds and the features of the phase transition they manifest.

1.4 Mott Insulators and Insulator-to-Metal Transitions

According to the classical band theory of solids (briefly introduced in Sec. 1.3), the insulating behaviour occurs in the case of crystals with an even number of electrons: in the simplest picture, corresponding to the two-band model, the completely filled band originates from the atomic orbitals, which are fully occupied by two electrons per orbital. On the other hand, system with an odd number of electrons should manifest a metallic behaviour, see Fig. 1.18a [Imada et al., 1998, Kittel, 2005, Ronchi et al., 2018]. However, this model does not allow to describe the properties of many transition metal oxides with partially filled d -orbitals, in which electrons are subjected to both localizing (Coulombic repulsion) and delocalizing (hybridization with the oxygen p electron states) forces [Tokura, 2003]. For these materials an insulating behaviour was reported [Imada et al., 1998] despite an odd number of electrons per unit cell. In order to successfully describe this observations, the role of electron-electron interactions should be taken into account. Indeed, in these insulating compounds (named Mott insulators after the work by Mott [Mott, 1949]) the strong Coulomb repulsion (U), between the two electrons occupying the same orbital, leads to the opening of a gap (called *Mott gap*) and to the formation of two characteristic bands: a full Lower Hubbard Band (LHB) and an empty Upper Hubbard Band (UHB), separated by U ($\sim 1 - 10$ eV in transition metal oxides [Zhou and Ramanathan, 2013]), see Fig. 1.18b [Ronchi et al., 2018]. In particular, when the U overcomes the kinetic energy, *i.e.* bandwidth $W =$

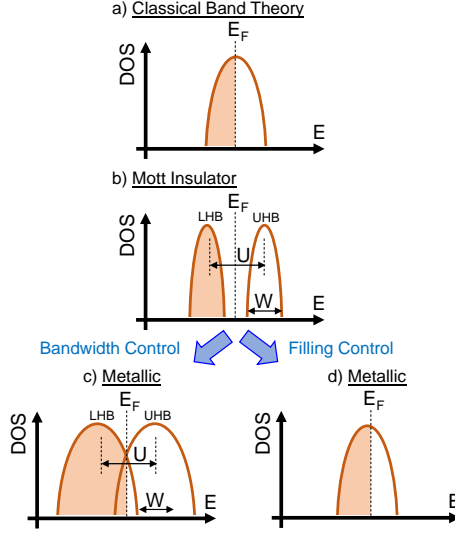


Figure 1.18: **Mott Transition**. (a) According to the classical band theory, a metal-like behaviour is predicted for those materials with partially filled orbitals. A non-zero density of state (DOS) at the Fermi level (E_F) characterizes the system. (b) In correlated materials, the strong electron correlations (U) split the original partially filled band into two: one filled (Lower Hubbard Band, LHB) and one empty (Upper Hubbard Band, UHB). (c, d) Band-control mechanisms allow to achieve the gap collapse: (c) bandwidth (W) and (d) filling control. Adapted from [Zhou and Ramanathan, 2015].

$4t$ (t is the hopping), electrons are hindered in forming bands or hopping through the lattice [Zhou and Ramanathan, 2015]. Therefore, in the case of one electron per site, the LHB is completely filled and the system exhibits an insulating behaviour although having an odd number of electrons in the unit cell [Imada et al., 1998]. When the temperature overcomes a certain threshold, which depends on the energy scale of the electronic correlations and on the interplay between localizing and delocalizing forces, the material can exhibit a metallic behaviour [Zhou and Ramanathan, 2013, Ronchi, 2020].

In general, the interplay between charge, spin, and orbital degrees of freedom play an important role in the insulator-to-metal transition [Tokura et al., 2017], labelled *Mott transition* [Tokura, 2003] in the case of these compounds. This transition can be achieved via two different mechanisms: bandwidth (BC) and band-filling (FC) control, see Fig. 1.18c and d. In the former, a variation of the effective electron correlation strength (U/W), which is typically achieved by changing the atomic spacing thanks to an external stress [Zhou and Ramanathan, 2013, Zhou and Ramanathan, 2015], drives the Mott

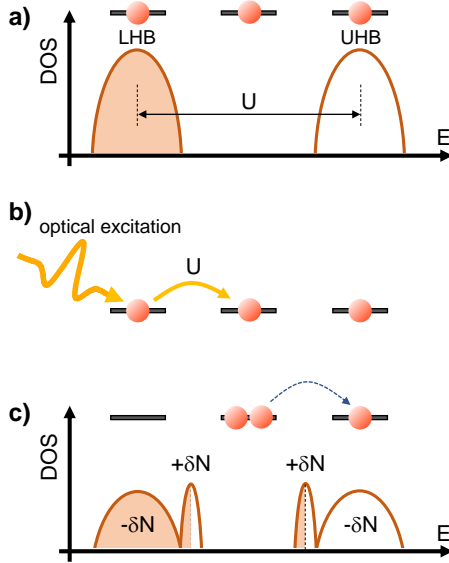


Figure 1.19: **Photoexcitation Process in Mott Insulator.** (a) Mott insulator at half-filling occupation ($n = 1$): each site is singly occupied. (b) An optical excitation (greater than U) creates holes and doublons. (c) Electron-hole excitations move freely throughout the lattice due to the appearance of metal-like states. Adapted from [Ronchi et al., 2018].

transition at a critical value U_c . On the latter case, a carrier-doping mechanism is pursued by adding electrons/holes to the system [Zhou and Ramanathan, 2015], *via* chemical, electrostatic, and photo-induced doping [Tokura et al., 2017]. Indeed, at half filling ($n = 1$, [Imada et al., 1998]), Coulomb repulsion prevents the electrons from hopping to another singly occupied site (see Fig. 1.19a). However, if the the system is doped with electrons, some sites becomes doubly occupied and, thus, electrons can move freely towards a singly occupied site (since there is no energy variation before and after hopping) [Zhou and Ramanathan, 2013].

For our purposes, it is useful to briefly describe the case of photo-induced FC control of the Mott transition. When a Mott insulator is exposed to light, the equilibrium charge distribution within the bands is modified, without changing the carrier density [Zhou and Ramanathan, 2013, Ronchi et al., 2018]. Any photo-induced electron-hole excitation, at the energy cost U (see Fig. 1.19b), creates additional conductive states (holes and doublons) which can move throughout the lattice at zero energy cost. The emergence of these low-energy metal-like states is accompanied by the decrease of the spectral weight of

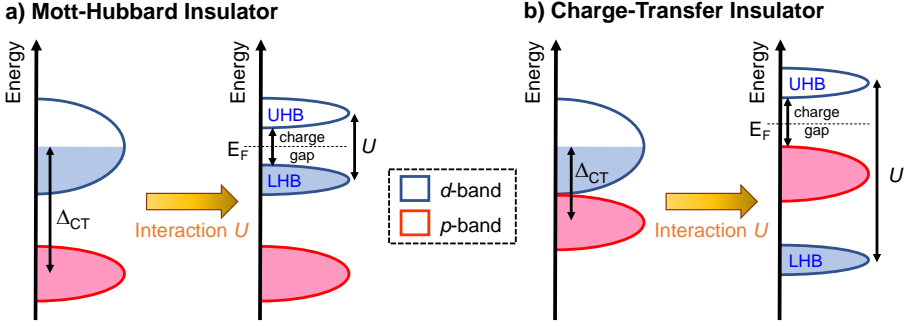


Figure 1.20: **Mott-Hubbard and Charge-Transfer Insulator.** Sketch of the energy levels for (a) a Mott-Hubbard insulator and (b) Charge-Transfer insulator. LHB: Lower-Hubbard Band; UHB: Upper-Hubbard Band. Adapted from [Imada et al., 1998].

electronic bands at the energy scale U (Fig. 1.19c) [Ronchi et al., 2018]. In this context, a suitable light excitation can be employed to determine the collapse of the Mott gap and, therefore, to induce the phase transition between two phases which are thermally accessible. Therefore, light represents an external control parameter to drive the IMT in correlated materials [Zhang and Averitt, 2014, Basov et al., 2017].

Before describing the case of photo-induced phase transition in a correlated material, it is useful to specify few concepts related to the description of Mott insulators and to low-energy excitations injected in these compounds. The prototype theoretical description of the transition between the Mott-insulator and metal is known as *Hubbard model* [Hubbard and Flowers, 1963], which considers a simplified lattice fermion model where electrons occupy a single orbit thus neglecting multiband effects [Imada et al., 1998]. However, the orbital degeneracy represents an important feature for d -electron systems (transition-metal compounds), whose IMT had been systematically studied under an experimental point of view. Another aspect related to multiband effect, which occurs, for example, in the case of transition-metal oxides involving heavier compounds such as Ni or Cu, is due to the presence of the oxygen p band of the ligand atoms near the partially filled d band of the transition-metal. In this case, the charge gap of the Mott insulator results from the interplay between the d and p -electrons degrees of freedom. Fig. 1.20a displays the condition in which the oxygen p level lies at energy ε_p well below the d level (located at ε_d). In this case, the Coulomb repulsion is lower than the charge transfer energy, $\Delta_{CT} = |\varepsilon_p - \varepsilon_d|$ and it determines the charge gap in the Mott-insulating phase. In this case, labelled as *Mott-Hubbard insulator*, $U < \Delta_{CT}$ and the low-energy excitations have character d . On the other hand (as depicted in Fig.

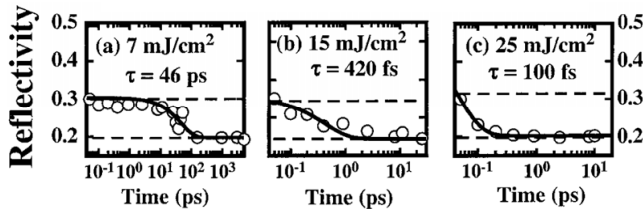


Figure 1.21: **Photo-induced Phase-Transition in VO₂**. Reflectivity as a function of the time delay between the pump and the probe, for different fluences: (a) 7 mJ/cm², (b) 15 mJ/cm², and (c) 25 mJ/cm². The value of the transition time has been obtained by fitting an exponential curve (solid black line) to the experimental data (markers). Adapted from [Cavalleri et al., 2001].

1.20b), when the the oxygen p level is located close to the d level, the charge transfer is responsible for the charge gap opening. In this *Charge-Transfer* insulator ($\Delta_{CT} < U$), the low-energy excitation assumes a strongly hybridized p - d character [Imada et al., 1998].

Within transition metal oxides family exhibiting insulator-to-metal transitions, the photo-induced IMT in the vanadium oxide VO₂ gathered an increasing scientific interest in the lasts three decades [Zhou and Ramanathan, 2015] and it has been investigated with various time-domain techniques [Giannetti et al., 2016], such as pump-probe spectroscopy [Cavalleri et al., 2001, Cavalleri et al., 2004, Wall et al., 2012, Morrison et al., 2014], time-resolved X-ray [Cavalleri et al., 2001] and electron diffraction [Morrison et al., 2014]. At equilibrium, starting from the monoclinic (M_1) insulating phase at room temperature, VO₂ undergoes a first-order phase transition towards the rutile (R) metallic phase above the critical temperature $T_c \sim 343$ K [Cavalleri et al., 2001, Cavalleri et al., 2004, Wall et al., 2012].

The first important investigation of the photo-induced phase transition occurring in this compound was conducted by Cavalleri and coworkers thanks to a space- and time-resolved pump-probe approach, in which a 200-nm VO₂ film sample is excited by a 50-fs optical pump at 800 nm [Cavalleri et al., 2001]. In this work, they demonstrated that, upon photo-excitation the insulating phase, the out-of-equilibrium reflectivity changes with time delay and, eventually, it reaches the equilibrium value of the metallic phase, see Fig. 1.21 [Cavalleri et al., 2001]. Interestingly, the time necessary to reach the metallic phase (transition time) decreases from more than 50 ps to about 100 fs as the pump fluence increases [Cavalleri et al., 2001]. In particular, between 10 and 12 mJ/cm², the transition time value decreases one order of magnitude from 10 ps to 0.9 ps [Cavalleri et al., 2001], thus suggesting the presence of a threshold.

In line with this experiment, time-resolved approach was widely employed to

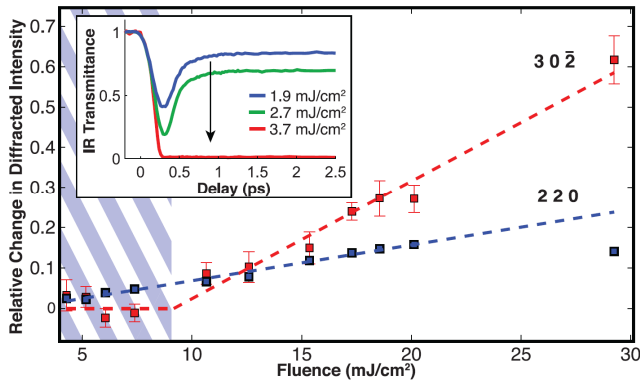


Figure 1.22: **Lattice and Electronic Contribution in VO₂ Photo-induced Phase Transition.** Relative variation of the signal amplitude as a function of the incident fluence for the (302) and (220) diffraction peaks (red and blue markers, respectively). The hatched region highlights the fluence range for which the structural phase transition is not observed. Inset: time-resolved transmittance at 5 μm (0.25 eV) probe wavelength for fluence values belonging to the hatched region. The measurements have been performed on a polycrystalline VO₂ film sample (70 nm) at $T \sim 310\text{ K}$. Adapted from [Morrison et al., 2014].

investigate the photo-induced phase transition in VO₂, since this method is capable to disentangle, in the time domain, the relative contributions of the electron-lattice interactions from the electron-electron interactions (which are responsible for the insulating phase) [Morrison et al., 2014, Giannetti et al., 2016]. One of the most recent and notable studies was conducted by Morrison and coworkers, in which the insulating phase of VO₂ is triggered by an ultrafast (35 fs) optical (800 nm) pump pulse and its out-of-equilibrium properties are detected by both ultrafast electron diffraction and infrared spectroscopy, addressing lattice and electronic properties, respectively [Morrison et al., 2014]. Thanks to the effective combination of these techniques, the properties of the photo-induced phase transition in VO₂ were rationalized according to the following scheme [Giannetti et al., 2016]:

- Above $\sim 9\text{-mJ/cm}^2$ excitation, the system undergoes a transition along a non-thermal pathway which melts the M_1 phase. In this high-fluence regime, the non-thermal transition is driven by a variation of the symmetry of the lattice potential originating from the prompt light-induced redistribution of charges in the solid, as suggested by the variation of diffracted intensity displayed in Fig.1.22 [Wall et al., 2012].
- Upon photo-excitation at intermediate fluences ($2 - 9\text{ mJ/cm}^2$), the system is driven to a transient metallic state (not accessible in equilibrium

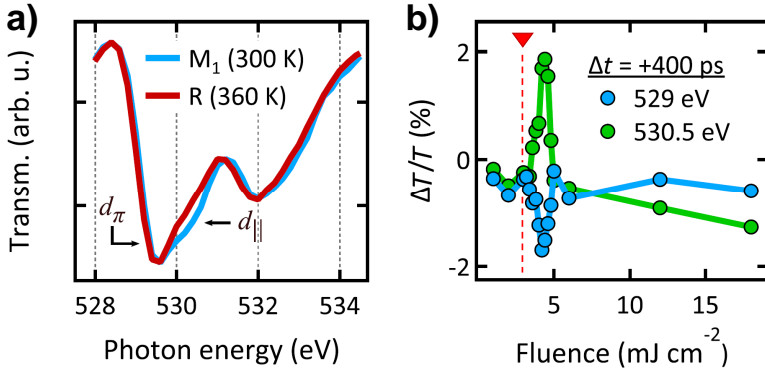


Figure 1.23: **X-ray Absorption Features at VO₂ Phase Transition.** (a) Static absorption spectra for the insulating (M₁, light blue solid curve) and metallic (R, red solid line) phases. (b) Fluence-dependent signal of π^* (529 eV, light blue solid line) and d_{\parallel} (530.5 eV, red solid line) states, taken at 400 ps time delay after excitation (70-ps time resolution). The dashed solid line denotes the insulator-to-metal transition threshold (3 mJ/cm²). The sample, polycrystalline VO₂ film (70 nm) deposited onto a freestanding Si₃N₄ membrane (150 nm), were measured in transmission configuration. Adapted from [Vidas et al., 2020].

conditions) characterized by the optical properties of the high-temperature phase (see inset in Fig. 1.22) and by the crystallographic structure of the low-temperature one (hatched region in Fig. 1.22). Indeed, for this fluence regime, the excitation level is not high enough to initiate the structural phase transition; however, it is capable to reorganize the carriers from the localized V-3d valence states of the insulating phase thus leading to an instantaneous collapse of the Mott gap [Morrison et al., 2014].

At this stage, it must be emphasized that the nature of the ultrafast phase transition is still the subject of an intense study [Vidas et al., 2020]. The crucial point of the strong debate is related to the understanding of the deep character of the fluence threshold, namely whether it represents the critical value of the energy density or that of the excited electron density, and its connection with the thermal energy of the phase transition [Vidas et al., 2020].

In this context, one of the most recent investigation was conducted by Vidas and coworkers [Vidas et al., 2020] after observing that systematic errors in the evaluation of the fluence threshold (concerning the electronic and structural transition) may occurs due to the comparison of results obtained by different experimental setups [Vidas et al., 2020]. In order to overcome this limitation, Vidas and coworkers employed X-ray absorption spectroscopy (XAS), a technique which is sensitive simultaneously to both electronic and structural changes. Fig.

1.23 summarizes the at- and out-of-equilibrium properties (panels a and b, respectively) of the absorption features at the oxygen K -edge of VO_2 : π^* (at 529 eV) and d_{\parallel} (at 530.5 eV) states, as displayed in Fig. 1.23a [Vidas et al., 2020]. These features, which arise from the strong covalent hybridization between oxygen $2p$ and vanadium $3d$ levels, allows to monitor the electronic (π^*) and structural (d_{\parallel}) properties of VO_2 across the transition [Vidas et al., 2020].

In the transient regime, the XAS signal from the π^* and d_{\parallel} states, reported in Fig. 1.23b, suggests the presence of a single fluence threshold for both degrees of freedom. Indeed, the fluence-dependent signal at both probe energies, taken at 400 ps after excitation, exhibits a change in amplitude at the same fluence value (3 mJ/cm², dashed red line in Fig. 1.23b). For higher fluence values, the character of the signal amplitudes evolves in a similar way. Therefore, the presence of a single fluence threshold for the insulator-to-metal transition (3 mJ/cm²) suggests that the electronic and structural transitions are coupled [Vidas et al., 2020]. In line with this, Vidas and coworkers demonstrated that the amount of energy required to induce the phase transition upon light excitation is comparable to that need according to the thermal pathway (whose value is 432 J/cm³) [Vidas et al., 2020].

To conclude this section, we underline that the photo-induced phase transition discussed previously are based on an *incoherent* mechanism, in which the pump excitation modifies the orbital population and, consequently, the potential profile experienced by the electrons and the lattice. Another approach, in which the orbital population is *coherently* manipulated by suitable phase-coherent light pulses, addresses the coherence of the electronic degree of freedom as an additional control parameter for the insulator-to-metal transition.